SARS-CoV-2 neurotropism-induced anxiety and depression-like behaviors require Microglia activation

Qian Ge [1#], Shan Zhou [2#], Jose Porras [2], Panfeng Fu[4], Ting Wang[5], Jianyang Du[1,3] *, Kun Li[2] *

Author affiliations:
[1] Department of Anatomy and Neurobiology, University of Tennessee Health Science Center, Memphis, TN 38163, USA.
[2] Florida Research and Innovation Center, Cleveland Clinic, Port St. Lucie, FL 34987, USA
[3] Neuroscience Institute, University of Tennessee Health Science Center, Memphis, TN, United States.
[4] Center for Translational Science, Florida International University, Port St. Lucie, FL, 34987, USA

*** Correspondence to:**

Kun Li
Florida Research and Innovation Center,
Cleveland Clinic,
Port St. Lucie, FL 34987, USA
Tel:772-419-2239
E-mail:lik11@ccf.org

Jianyang Du
Department of Anatomy and Neurobiology,
University of Tennessee Health Science Center,
Memphis, TN 38163, USA
Tel: 901-448-3463
E-mail: jdu15@uthsc.edu

Authorship note: [#] G.P. and S.Z. contributed equally to this work.

KEYWORDS COVID-19, SARS-CoV-2, long COVID, post-acute sequelae of SARS-CoV-2 infection, spike protein, Microglia, Amygdala, neurotropism, anxiety- and depression-like behaviors, synaptic transmission and plasticity.

ABSTRACT

The coronavirus disease 2019 (COVID-19) pandemic, caused by severe acute respiratory syndrome coronavirus 2 (SARS-CoV-2), has been associated with a wide range of “long COVID” neurological symptoms. However, the mechanisms governing SARS-CoV-2 neurotropism and its effects on long-term behavioral changes remain poorly understood. Using a highly virulent mouse-adapted SARS-CoV-2 strain, denoted as SARS2-N501Y$_{MA30}$, we demonstrated that intranasal inoculation of SARS2-N501Y$_{MA30}$ results in viral dissemination to multiple brain regions, including the amygdala and hippocampus. Behavioral assays show a significant increase in anxiety- and depression-like behaviors 14 days following viral infection. Moreover, we observed microglia activation following SARS2-N501Y$_{MA30}$ infection, along with an augmentation in microglia-dependent neuronal activity in the amygdala. Pharmacological inhibition of microglial activity subsequent to viral spike inoculation mitigates microglia-dependent neuronal hyperactivity. Furthermore, transcriptomic analysis of infected brains revealed

the upregulation of inflammatory and cytokine-related pathways, implicating microglia-driven neuroinflammation in the pathogenesis of neuronal hyperactivity and behavioral abnormality. Overall, these data provide critical insights into the neurological consequences of SARS-CoV-2 infection and underscore microglia as a potential therapeutic target for ameliorating virus-induced neurobehavioral abnormalities.

INTRODUCTION:

As of September, 21th, 2023, the global pandemic of COVID-19 has resulted in 70,778,396 reported cases and 6,958,499 confirmed deaths (WHO COVID-19 Dashboard). The death rate and hospital admissions related to COVID-19 have been dramatically reduced as a result of extensive vaccination rollouts and improved treatments. However, a substantial number of patients (10-20%) are experiencing a persistent or newly developed set of symptoms following the acute phase of the illness. This condition is commonly referred to as "long COVID," also known as post-acute sequelae of SARS-CoV-2 infection (PASC) (1). While PASC initially attracted attention for its severe impact on older adults and those with underlying health concerns, it has since been clear that it may also occur in otherwise healthy young people, and it can develop after even a modest initial infection (2, 3). These long-lasting symptoms may persist for weeks or even months, posing challenges for healthcare providers and necessitating further research and support to address the long-term health consequences of the disease.

Among the enduring symptoms of PASC, neurological manifestations stand out prominently. Symptoms include cognitive difficulties, autonomic dysfunction, extreme fatigue, sleep disturbances, and mental health complications such as anxiety and depression (2, 3). The exact cause of these syndromes remains uncertain and is constantly being studied. Possible factors contributing to these symptoms include viral infection of brain cells, immune-mediated phenomena, coincidental events, or a combination of these factors. In vitro studies have provided clear evidence of SARS-CoV-2 infection in human brain organoids or cell cultures (4, 5) Additionally, several autopsy studies have reported the presence of viral RNA or proteins in the brains of patients who died from COVID-19, suggesting the possibility of SARS-CoV-2 neurotropism in the central nervous system (CNS) (5, 6). The neuromechanism of SARS-CoV-2 is not clearly defined, both a systematic mechanism and direct neurotropism have been proposed (7). Recent studies suggest that SARS-CoV-2 triggered the COVID-19 pandemic, and possesses brain neurotropism primarily through binding to the ACE2 on neurons (5), or through tunneling nanotubes (8). In addition to direct invasion of neuronal cells, the activation of microglia and/or astrocytes might contribute to the onset and progression of neurological disorders through abnormal maintenance of homeostasis, leading to altered neuronal activities, and thus is considered critical in defining the neurological damage and neurological outcome of COVID-19 (9).

As the principal innate immune cells of the brain, microglia form the primary focus of research in the field of neuroimmune disease. Microglia are the most dynamic neural cells found to date (10-12). Their profoundly dynamic processes constantly survey the

local microenvironment, monitor neuronal activity (13, 14), and respond to infection and injury by releasing pro-inflammatory molecules and phagocytic clearance of apoptotic cells (15). During a homeostatic situation, secretion of molecules and phagocytosis by microglia likewise maintain synaptic transmission and plasticity (16, 17). In contrast, hyperactive microglia can be pathogenic and are associated with symptoms of psychiatric disorders, including anxiety disorders and major depression (18), which have commonly appeared during the COVID-19 pandemic. The activity of microglia can be modulated by neuronal activity (19-21), suggesting the existence of microglia-neuron crosstalk. Despite the high potential relationship between SARS-CoV-2 infection and the neuroimmune system, the mechanisms by which SARS-CoV-2 infection activates pro-inflammatory microglia regulates microglia-neuron interaction and alters neuronal activity have not been adequately studied.

Further research is essential to comprehensively unravel the mechanisms underlying PASC and its neurological manifestations, as this knowledge is critical for developing effective management and treatment strategies for affected patients. Mouse models serve as invaluable tools in conducting such studies. Unfortunately, mice are naturally resistant to original SARS-CoV-2 infection due to the low affinity of the viral spike (S) glycoprotein to mouse ACE2 receptors (mACE2) (22, 23). To overcome this limitation, several strategies have been employed to overexpress human ACE2 (hACE2) in mice. These approaches include the delivery of exogenous hACE2 using a replication-deficient adenovirus (Ad5-hACE2) or Adeno-associated Virus (AAV-hACE2), and the generation of K18-hACE2 transgenic mice (24-26). These models have been used to investigate the acute infection of SARS-CoV-2 as well as the neurological consequences (5). However, it should be noted that these models have drawbacks that limit their application in studying long-term PASC after SARS-CoV-2 infection. The former may be incapable of getting a brain infection, whereas the latter may acquire severe artificial multiorgan infections with a high mortality rate, rendering them poor candidates for long-term post-infection behavioral testing.

Our research team and collaborators successfully isolated a highly virulent mouse-adapted SARS-CoV-2 strain, SARS2-N501Y$_{MA30}$, through serial passage of a recombinant SARS-CoV-2/spike N501Y virus in BALB/c mice (27). After SARS2-N501Y$_{MA30}$ infection, viral titers, viral genomic RNA (gRNA), and subgenomic RNA (sgRNA) were detected in the lungs and the brains, indicating the presence of virus infection in the C57BL/6 mice. Fourteen days after the SARS2-N501Y$_{MA30}$ infection, the mice displayed abnormal anxiety- and depression-like behaviors in multiple behavioral paradigms including the open-field test, elevated plus maze test, tail suspension test, and forced swimming test, supporting the conclusion that the SARS2-N501Y$_{MA30}$ infection causes the increase in anxiety- and depression-like behaviors in mice. We also found microglia activation after SARS2-N501Y$_{MA30}$ infection and increased microglia-dependent neuronal activity in the amygdala, <u>the critical brain region for anxiety and depression-like behaviors in rodents</u> <u>and humans</u> (28). Overall, our study indicates that microglial activation plays a pivotal role in inducing anxiety- and depression-like behaviors following SARS-CoV-2 infection in mice.

130 The evaluation of the consequences of N501Y$_{MA30}$ infection on the CNS has provided
131 valuable insights, positioning this mouse-adapted strain as an auspicious model for
132 studying the neurological manifestations of PASC. Continuation of research utilizing this
133 mouse model, alongside other relevant models, is pivotal in advancing our
134 understanding of the neurological effects of SARS-CoV-2 and facilitating the
135 development of effective interventions for PASC. Our findings uncover the neurotropic
136 potential of SARS-CoV-2 and its direct link to anxiety- and depression-like behaviors
137 through the activation of microglia-mediated neuroinflammatory pathways. This study
138 sheds information on the neurological repercussions of SARS-CoV-2 infection and
139 suggests microglia as prospective therapeutic targets for reversing virus-induced
140 neurobehavioral deficits. Understanding the neurological basis of COVID-19-related
141 neuropsychiatric symptoms is critical for developing effective treatment to reduce the
142 long-term PASC impact on mental health.

143 **MATERIALS AND METHODS**

144 **Mice, virus, and cells**

145 Specific pathogen-free 6-9 weeks male and female Balb/c and C57BL/6 mice were
146 purchased from the Jackson Laboratory. All protocols were approved by the Institutional
147 Animal Care and Use Committees of Cleveland Clinic-Florida Research and Innovation
148 Center (CC-FRIC) and the University of Tennessee Health Science Center (UTHSC).
149 The mouse-adapted SARS-CoV-2-N501Y$_{MA30}$ was provided by Drs. Stanley Perlman
150 and Paul McCray at the University of Iowa, USA (27). The virus was propagated in
151 Calu-3 cells and tittered by plaque assay in VeroE6 cells. Calu-3 cells were maintained
152 in minimal essential medium (MEM) supplemented with 20% fetal bovine serum (FBS),
153 0.1 mM nonessential amino acids (NEAA), 1 mM sodium pyruvate, 2 mM l-glutamine,
154 1% penicillin and streptomycin, and 0.15% $NaHCO_3$ at 37°C in 5% CO_2. Vero E6 cells
155 were grown in Dulbecco's modified Eagle medium (DMEM) supplemented with 10%
156 FBS, 0.1 mM NEAA, 1 mM sodium pyruvate, 2 mM l-glutamine, 1% penicillin and
157 streptomycin, and 0.15% $NaHCO_3$ at 37°C in 5% CO_2.
158

159 **Virus infection and titration.**

160 The research involving SARS-CoV-2 was conducted within the biosafety level 3 (BSL3)
161 Laboratory at CC-FRIC. Balb/c or C57BL/6 mice were gently anesthetized using
162 isoflurane and subsequently intranasally infected with 10^4 FPU of SARS-CoV-2-
163 N501Y$_{MA30}$. Post-infection, daily monitoring and weight measurements of the mice were
164 conducted. Tissues were aseptically collected and dissociated in PBS using disposable
165 homogenizers. The viral preparations and supernatants from lung or brain tissue
166 homogenates were subject to sequential dilution in DMEM. These diluted samples were
167 then introduced to VeroE6 cells in 12-well plates to conduct plaque assays (29). After
168 one hour of incubation, the viral inoculums were removed, and the cells were overlaid
169 with a 1.2% agarose solution supplemented with 4% FBS. After 3-day incubation, the
170 cells were fixed with formaldehyde, and the overlays were meticulously eliminated,
171 facilitating visualization of the resulting plaques through the application of a 0.1% crystal
172 violet stain.

173 **Behavioral experiments**
174 In this study, C57BL/6 mice aged 6-9 weeks were utilized to investigate behavioral
175 responses using a battery of tests as described in **Fig.5**. Briefly, the Open Field Test
176 assessed exploratory and anxiety behaviors in an open-field box for 5 minutes. The
177 Elevated Plus Maze evaluated anxiety-like behavior by recording entries into and time
178 spent in the open arms of a maze for 5 minutes. The Tail Suspension Test and Forced
179 Swimming Test were employed to assess depressive-like behavior, with mice
180 suspended by their tails for 6 minutes using adhesive tape in a controlled environment,
181 and the mice were placed in water-filled cylinders for 6 minutes, respectively. Immobility
182 time during specific intervals was measured in both tests. Ethical approvals were
183 obtained to ensure compliance with animal welfare guidelines.

184 **Quantitative real-time PCR analysis of viral RNA.**
185 Total cellular RNA was isolated using the Direct-zol RNA miniprep kit (Zymo Research,
186 Irvine, CA) following the manufacturer's protocol including a DNase treatment step.
187 Total RNA (200 ng) was used as the template for first-strand cDNA synthesis. The
188 resulting cDNA was used to quantify the SARS-CoV-2 RNA levels by real-time
189 quantitative PCR using Power SYBR green PCR master mix (Applied Biosystems,
190 Waltham, MA). Average values from duplicates of each sample were used to calculate
191 the viral RNA level relative to the GAPDH gene and presented as $2^{-\Delta CT}$, as indicated
192 (where CT is the threshold cycle). CT values of gRNA and sgRNA from uninfected mice
193 (0 dpi) are constantly>35. The sequences of the primers used are listed in the **S1 Table**.

194 **Brain slice preparation, S1 protein perfusion, and slice excitatory postsynaptic**
195 **potentials (EPSP) recording.**
196 Mice were euthanized with overdosed isoflurane and whole brains were dissected into
197 pre-oxygenated (5% CO_2 and 95% O_2) ice-cold high sucrose dissection solution
198 containing (in mM): 205 sucrose, 5 KCl, 1.25 NaH_2PO_4, 5 $MgSO_4$, 26 $NaHCO_3$, 1 $CaCl_2$,
199 and 25 Glucose and sliced into 300 μm on a Leica VT1000S vibratome (30). The
200 transverse hippocampal slices were then transferred into the normal artificial
201 cerebrospinal fluid (ACSF) containing (in mM): 115 NaCl, 2.5 KCl, 2 $CaCl_2$, 1 $MgCl_2$,
202 1.25 NaH_2PO_4, 11 glucose, 25 $NaHCO_3$, bubbled with 95% O_2/5% CO_2, pH 7.35 at
203 20°C-22°C. Slices were incubated in the ACSF at least 1 hour before recording.
204 Individual slices were transferred to a submersion-recording chamber and were
205 continuously perfused with the 5% CO_2/95% O_2 solution (~3.0 ml/min) at room
206 temperature (20°C - 22°C). The spike protein (BPSbioscience, #510333) was diluted to
207 200 ng/ml and perfused to the brain slices in the ACSF. For the field EPSP
208 experiments, neurons were held in current-clamp mode with a pipette solution
209 containing (in mM): 2 KCl (mOsm = 290, adjusted to pH 7.25 with KOH). A concentric
210 bipolar stimulating electrode (FHC Inc., Bowdoin, ME) was positioned in the middle of
211 the CA1 stratum radiatum near the CA3 side. Away from the stimulating electrode
212 around 400 μm is a glass recording electrode. EPSPs were recorded in current-clamp
213 mode every 20 seconds and continuously recorded the EPSPs for at least 1 hour. Data
214 were acquired at 10 kHz using Multiclamp 700B and pClamp 10.

215

216 **ATP measurement**
217 Mice were deeply anesthetized with isoflurane, followed by decapitated, and brains
218 were removed from the skull and dissected. Brain slices were then placed in 200 µl ice-
219 cold PBS, either in the absence or presence of spike protein (167 ng/ml, BPS
220 BIoscience, #510333) for the indicated time (10, 30, 60 minutes). To quantify ATP
221 released from the brain slice, we employed an ATP Determination kit (Invitrogen,
222 A22066). Briefly, a 100 µl reaction mixture was added to the 96-well cell culture plate,
223 which contains a 10 µl sample or standard solution. After 15 minutes of incubation in the
224 dark, the plate was read using a Synergy Neo2 hybrid multimode microplate reader
225 (BioTek, Winooski, VT, USA). ATP concentrations were determined by reference to a
226 standard curve.

227 **Histology.**
228 Tissues (lungs, brain) were collected and fixed in zinc formalin. Following fixation, the
229 lungs were processed for paraffin embedding and sliced into a 4 µm section and the
230 brain was sectioned into 30 µm by a vibratome for subsequent hematoxylin and eosin
231 (H&E) staining by Immunohistochemistry Core of Cleveland Clinic Lerner Research
232 Institute and Immunohistochemistry Core at the University of Tennessee Health Science
233 Center. We have used two serial lung sections (six fields/section) from each animal and
234 a total of 4 to 5 animals per group. Acute lung injury severity was evaluated with ATS
235 guidelines (31) for neutrophil infiltration in alveolar and interstitial space, hyaline
236 membranes, alveolar wall thickening, and proteinaceous debris deposition. Briefly, a
237 scoring system (0-2) was employed for each of the criteria mentioned. An average
238 score of 0 indicated absence of injury, 1 indicated mild to moderate injury, and 2
239 indicated severe injury.

240 **Immunohistochemistry**
241 Following the behavioral procedures indicated in the text and figures, the mice were
242 euthanized with overdosed isoflurane and were fixation in Zinc Formalin. Following
243 fixation, we used a vibratome (Leica VT-1000S) to dissect 30 µm amygdala coronal
244 slices, which were collected in ice-cold PBS. To complete immunofluorescence staining,
245 slices were placed in Superblock solution (Thermo Fisher Scientific) plus 0.2% Triton X-
246 100 for 1 hour and incubated with primary antibodies (1:1000 dilution) at 4°C for 24
247 hours (30). Primary antibodies we used include mouse monoclonal antibody to dsRNA
248 (Millipore Cat# MABE1134); Rabbit polyclonal to Iba1 (Abcam Cat# ab108539); Rabbit
249 polyclonal to GFAP (Abcam Cat# ab7260) and mouse anti-NeuN (Millipore Cat#
250 MAB377X). We then washed and incubated slices for one hour with secondary
251 antibodies (Alexa Fluor 488 goat anti-rabbit IgG (H+L) (Molecular Probes Cat# A-
252 11039); Alexa Fluor 594 goat anti-mouse IgG (H+L) (Thermo Fisher Scientific Cat# A-
253 11032); Alexa Fluor 647 goat anti-mouse IgG (H+L) (Thermo Fisher Scientific Cat# A-
254 21235), 1:200 dilution). VectaShield H-1500 (Vector Laboratories Cat# H-1500) was
255 used to mount slices, while regular fluorescent DIC microscopy and confocal
256 microscopy were used to image the slices.
257
258 For SARS-CoV-2 antigen detection, tissue slides underwent a series of incubation
259 steps. Initially, slides were treated with a blocking reagent (10% normal goat serum) for

30 minutes to reduce non-specific binding. Subsequently, a rabbit polyclonal antibody against the SARS-CoV-2 nucleocapsid protein (dilution: 1:4,000, catalog number: 40143-T62, Sino Biological) was applied to the slides for 15 minutes. Following the primary antibody incubation, slides were further incubated with Rabbit Envision (Dako) and diaminobenzidine (Dako) as a chromogen to visualize the antigen-antibody complexes.

Dendrites and spine morphologic analyses.
After their behavioral testing, we measured the density of dendritic spines on amygdala neurons by using Golgi staining (n = 5 per group). Mice brains were collected, fixed and processed for the Golgi staining according to the protocol provided by the FD Rapid Golgi Stain Kit (PK401, FD NeuroTechnologies). All images were deconvolved within the Zeiss Application Suite software. The number of dendritic spines was analyzed using plug-in SpineJ as described (32), with modifications. Spines were examined on dendrites of amygdala neurons that satisfied the following criteria: (1) presence of untruncated dendrites, (2) dark and consistent Golgi staining throughout all dendrites, and (3) visual separability from neighboring neurons. We counted the number of dendritic spines along the second dendritic branch at distances from 50 to 100 μm from the soma, in images obtained at 630× magnification. For each neuron, three to five dendritic segments 10 μm in length were analyzed. For each group, 6-10 neurons/mice were analyzed. We used ImageJ software to analyze spines. The analysis of dendritic spines includes the number of spines and spine density, which are critical indicators of synaptic function (33, 34). Spines were classified as thin if they had a long, slender neck and small, Spine length > 0.5 μm; Head perimeter = 2 μm to 3 μm; mushroom, if they had a well-defined, thick neck and spine length > 0.5 μm; Head perimeter ≥ 3 μm; or stubby, if they were short and thick, without a distinguishable neck, spine length ≤ 0.5 μm; or filopodia if they were long and curved, spine length > 0.5 μm, head perimeter ≤ 2 μm.

Statistical analysis.
One-way ANOVA and Tukey's post-hoc multiple comparison tests were used for statistical comparison of groups. An unpaired Student's t-test was used to compare results between the two groups. $p < 0.05$ was considered statistically significant, and we did not exclude potential outliers from our data except the ones that did not receive successful aversive conditioning. The graphing and statistical analysis software GraphPad Prism 8 was used to analyze statistical data, which was presented as means ± SEM. Sample sizes (n) are indicated in the figure legends, and data are reported as biological replicates (data from different mice, and different brain slices). Each group contained tissues pooled from 4-5 mice. Due to variable behavior within groups, we used sample sizes of 10-16 mice per experimental group as we previously described in earlier experiments (30). In behavioral studies, we typically studied groups with five randomly assigned animals per group. The experiments were repeated with another set of four animals until we reached the target number of experimental mice per group.

RESULTS

Neuroinvasion following Respiratory Infection of SARS-CoV-2

306 The inherent low affinity of the viral spike (S) glycoprotein for mouse ACE2 (mACE2)
307 renders mice naturally resistant to original SARS-CoV-2 infection (22, 23). However,
308 specific mutations in the viral spike protein, such as Q498Y, P499T, and N501Y, can
309 enhance binding to mACE2, resulting in asymptomatic infection in mice(35). Through
310 serial passages of a recombinant SARS-CoV-2/spike N501Y virus in BALB/c mice, we
311 successfully isolated a highly virulent mouse-adapted SARS-CoV-2 strain, designated
312 as SARS2-N501Y_{MA30} (27). Interestingly, young C57BL/6 mice exhibited reduced
313 sensitivity to symptomatic infection by SARS2-N501Y_{MA30} **(Fig. 1A)**, making them an
314 optimal model for studying the long-term repercussions of COVID-19. Thus, we
315 intranasally infected mice with 10^4 PFU/mouse of SARS2-N501Y_{MA30} (27). Comparable
316 to our previous findings, young Balb/c mice developed lethal disease **(Fig. 1B, C)**,
317 whereas young C57BL/6 mice only displayed minimal weight loss of less than 20% and
318 swift recovery within approximately one week **(Fig. 1B, C)**. In C57BL/6 mice, viral titers
319 peaked at 2 days post infection (dpi) in the lungs, followed by the presence of viral titers
320 in the brain peaking at 4 dpi **(Fig. 1D, E)**. Consistent with the observation, both viral
321 genomic RNA (gRNA) and subgenomic RNA (sgRNA) were identified in the lung
322 **(Supplemental Fig.1)** and brain **(Fig. 1F, G)**. Immunofluorescence targeting double-
323 stranded RNA (dsRNA) further validated replicative virus presence in amygdala brain
324 slices at 4 dpi **(Fig. 1H-I)**, with similar observations in the prefrontal cortex, albeit with
325 slight distinctions **(Fig. 1K)**. These results collectively suggest direct viral infiltration into
326 the brain, alongside respiratory infection. Remarkably, the production of infectious
327 SARS-CoV-2 appeared to be controlled in the brain, as the titer is extremely low **(Fig**
328 **1E)** and it did not induce major pathological changes within brain tissues
329 **(Supplemental Fig. 2**). Consistent results were found in the qPCR for viral RNA and
330 immune-fluorescence targeting dsRNA **(Fig. 1)**. These findings indicated a SARS2-
331 N501Y_{MA30} neuroinvasion with a peak at 4 dpi followed by a quick clearance.
332
333 Histological analysis of lung samples revealed acute lung injury using American
334 Thoracic Society (ATS) guidelines for experimental acute lung injury (ALI) based on
335 neutrophil infiltration in alveolar and interstitial space, hyaline membranes, alveolar wall
336 thickening, and proteinaceous debris deposition (31). SARS-CoV-2 infection induced
337 markedly increased lung injury which peaked on day 6, accompanied by viral antigen
338 presence at 2 dpi and disappeared after 6 dpi **(Supplemental Fig 3)**. However, these
339 changes, including infiltration and viral presence, resolved after a 14-week period. To
340 explore the innate immune and host defense responses in SARS-CoV-2-infected mice,
341 we assessed cytokine/chemokine gene expression in the lungs **(Supplemental Fig 1)**.
342 Notably, these genes exhibited significant upregulation at 2 dpi or 4 dpi, gradually
343 subsiding to baseline levels after 6 dpi. These findings collectively illustrate a mild-to-
344 moderate respiratory disease in the infected lungs, which subsequently resolved within
345 14 days post-infection.
346
347 **SARS2-N501Y_{MA30} infection induces significant changes in anxiety- and**
348 **depression-like behaviors.**
349 Our investigation successfully detected viral dsRNA within the amygdala/pre-frontal
350 cortex region **(Fig. 1K)**-an area pivotal in learning and coordinating defensive responses
351 (36). This finding prompted us to postulate that the infection may still exert influence
352 over the functionality of this region and consequently modify the defensive behaviors of

353 infected mice. To evaluate the impact of SARS-CoV-2 infection on anxiety- and
354 depression-like behaviors, we conducted a well-established behavioral test battery in
355 mice fourteen days after intranasal administration of SARS2-N501Y$_{MA30}$ (10^4 PFU/
356 mouse) **(Fig. 2A)**. In the open-field test, the infected mice exhibited a decreased
357 duration spent in the center area compared to the mock infection group, indicative of
358 heightened anxiety-like behaviors **(Fig. 2B, left)**. Remarkably, both the SARS2-
359 N501Y$_{MA30}$ and mock infection groups demonstrated similar locomotor activity, implying
360 a complete recovery of locomotion post-infection **(see Fig. 2B, right)**. In the elevated
361 plus-maze test, mice in the infected group significantly reduced their time spent in the
362 open arms **(Fig. 2C, left)**, while the number of entries into the open arms remained
363 unaltered **(Fig. 2C, right)**, further substantiating an augmentation in anxiety-like
364 behaviors. Consistent outcomes were observed in the tail suspension and forced
365 swimming tests, both are widely used for evaluating depression-like behaviors, where
366 mice in the virus-infected groups displayed increased immobile time compared to the
367 vehicle groups **(Fig. 2D, E)**. These findings collectively substantiate our conclusion that
368 SARS2-N501Y$_{MA30}$ infection leads to an upsurge in anxiety-and depression-**like**
369 behaviors in mice and the alterations in the anxiety-and depression-like behaviors
370 suggest potential repercussions on brain function, warranting further exploration.
371
372 **Spike protein increases microglia-dependent field EPSPs (fEPSPs) in amygdala**
373 **slices**
374 Exposure to the SARS-CoV-2 spike protein has emerged as a topic of interest in
375 neurobiology, particularly regarding its impact on neuronal function. Previous research
376 has provided initial insights into how spike protein can influence neuronal morphology
377 and function (37-39). In this study, we aimed to delve deeper into the mechanistic
378 aspects of this phenomenon, focusing on the amygdala, a region critically involved in
379 emotional processing and defensive behaviors. we perfused amygdala slices from mice
380 with the recombinant B1.351 variant spike protein (200 ng/ml), which has a high affinity
381 to mouse ACE, and monitored changes in fEPSPs for 2 hours **(Fig. 3A)**. We revealed a
382 significant increase in fEPSPs following exposure to the B1.351 variant spike protein
383 **(Fig. 3 B, C)**, indicating heightened synaptic transmission and neuronal excitability.
384 Despite the fact that whether SARS-CoV-2 spike protein increases or decreases
385 neuronal activity is controversial (37-40). this observation is noteworthy, as it suggests
386 that the spike protein, when directly interacting with neurons, has the potential to amplify
387 their responsiveness to incoming signals. This heightened neuronal response could, in
388 turn, render individuals more sensitive to various stimuli, potentially leading to
389 alterations in behaviors or physiological reactions.

390 Interestingly, the administration of 50 μM Resveratrol, a known inhibitor of microglial
391 activation (41), effectively counteracted the spike protein-induced enhancement of
392 fEPSPs **(Fig. 3C, D)**. This finding suggests that microglia, the resident immune cells in
393 the brain, may play a pivotal role in mediating the effects of the spike protein on
394 neuronal activity.
395
396 **SARS2-N501Y$_{MA30}$ infection induces spine remodeling in the amygdala.**
397 To further validate the impact of SARS2-N501Y$_{MA30}$ infection on synaptic plasticity, we
398 subsequently investigated dendritic spine remodeling following SARS2-N501Y$_{MA30}$

399 infection. Dendritic morphology has been widely implicated in the mechanisms
400 governing synaptic plasticity (34, 42, 43). Dendritic spines constitute the principal target
401 of neurotransmission input within the CNS (44), and their density and structure form the
402 foundation for physiological alterations in synaptic efficacy that underlie learning and
403 memory processes (45). We hypothesized that dendritic structure and plasticity undergo
404 alterations following SARS2-N501Y_{MA30} infection. Fourteen days after nasal infection
405 with SARS2-N501Y_{MA30} **(Fig. 4A)**, brain slices containing the amygdala were
406 meticulously dissected, fixed, and subjected to Golgi staining to label the spines.
407 Neurons were randomly selected from within the basolateral amygdala, with a focus on
408 secondary branches located 50-100 μm away from the soma **(Fig. 4B, C)**.
409 Subsequently, spine morphology was manually visualized and analyzed **(Fig. 4D)**.
410
411 To characterize spine morphology, we categorized dendritic processes into two distinct
412 morphological classes: mature and immature spines (46). Mature spines, predominantly
413 exhibiting a "mushroom-like" morphology, exhibit more stable postsynaptic structures
414 enriched in AMPARs and are considered functional spines. Conversely, immature
415 spines, characterized by their thin, stubby, and filopodial features, represent unstable
416 postsynaptic structures with transitional properties. Immature dendritic spines are
417 believed to hold the potential for future synaptic plasticity, either maturing into functional
418 spines or disappearing from the dendrite (47). Spine categories were identified based
419 on parameters described in previous studies and Methods (34, 48).
420
421 We found variations in spine subtypes, including an increased percentage of mature
422 spines in neurons infected with SARS2-N501Y_{MA30} (14 dpi) compared to the mock
423 infection group **(Fig. 4E)**. This finding suggests heightened neuronal plasticity in
424 neurons following SARS2-N501Y_{MA30} infection. When combined with the data in **Fig. 3**
425 and dendritic morphology, our results indicate that synaptic plasticity is enhanced in
426 amygdala neurons fourteen days after SARS2-N501Y_{MA30} infection.
427
428 **Microglia activation after SARS-CoV-2 infection and exposure to spike protein**
429 Following up on the above finding in **Fig. 3**, we conducted further investigations into
430 microglial reactivity during SARS2-N501Y_{MA30} infection. We employed
431 immunofluorescence staining of Iba1, which allowed us to unveil their activation
432 characterized by a transition from a ramified to an amoeboid morphology (49). This
433 transition reached its peak at 4 days post-infection and disappeared at 14 days post-
434 infection, as illustrated in **Fig. 5A**. This finding provides supporting evidence that
435 microglial activation may contribute to the altered neuronal activities observed in the
436 amygdala after SARS-CoV-2 infection.
437
438 Microglia are dynamic cells that interact with both neurons and non-neuronal cells upon
439 activation, and their processes extend to target other brain cells (50). Understanding
440 these intricate interactions is essential to comprehending the impact of SARS-CoV-2
441 infection on the brain's immune response. We further investigated the mechanism by
442 which the spike protein promoted microglia activation. We visualized microglia in mouse
443 amygdala slices by immunofluorescence staining of Iba1 and found the activation of
444 microglia after SARS-CoV-2 B1.351 spike protein perfusion **(Fig. 5B, C)**. Interestingly,

445 inhibition of the purinoceptor $P2Y_{12}$ (P2Y12R) by ticlopidine mitigated these effects **(Fig.**
446 **5C, D)**. This finding suggests that microglial activation in response to the SARS-CoV-2
447 spike protein is mediated by the $P2Y_{12}R$ signal pathway, providing valuable insights into
448 the mechanisms underlying neuroimmune responses during SARS-CoV-2 infection.
449 $P2Y_{12}$ is a type of purinergic receptor, specifically a G protein-coupled receptor, that is
450 selectively expressed in microglia (51) and involved in mediating responses to
451 extracellular nucleotides like adenosine triphosphate (ATP) and adenosine diphosphate
452 (ADP). ATP plays a pivotal role as a chemoattractant released from neurons, effectively
453 triggering the activation and subsequent accumulation of microglia (19, 52).
454 Furthermore, the ATP-induced activation of microglia can, in turn, stimulate their
455 targeted neurons (16, 17). This suggests that ATP, known for its swift release from
456 activated neurons (53), may serve as a rapid responder to SARS2-N501Y_{MA30} infection.
457 Additionally, it is worth noting that SARS-CoV-2 infection has been shown to induce
458 ATP release from host cells, including neural cells, via ATP-release channels (54, 55).
459 Indeed, we found significantly increased ATP release in brain slices induced by spike
460 protein **(Fig. 5F, G)**.
461
462 **Brain Immune Inflammation and Anti-Viral Responses during Viral Infection**
463 Cytokines and chemokines serve as crucial indicators of anti-viral response and
464 immune inflammation. To delve into the immune responses within the brain during viral
465 infection, we conducted quantitative reverse-transcription PCR (RT-qPCR) to scrutinize
466 the expression of cytokines and chemokines across the entire brain **(Fig. 6)**.
467 Surprisingly, we found that the expression levels of interferon genes, including IFN-β, γ,
468 and λ, as well as the tumor necrosis factor gene, remained unaltered in the infected
469 brain tissues. However, it is noteworthy that transcripts encoding pro-inflammatory
470 cytokines, such as interleukin-1a (IL-1a), interleukin-6 (IL-6), interleukin-8 (IL8/CXCL1),
471 and especially monocyte chemoattractant protein-1 (MCP1/CCL2), exhibited significant
472 upregulation at 2- or 4-days post-infection. These temporal increases coincided with the
473 levels of viral RNA detected in the brain. Importantly, it is worth highlighting that the
474 alterations observed in immune gene expression within the brain were relatively modest
475 in comparison to those observed in the lungs and returned to normal levels after 6 days
476 post-infection. This discovery underscores the presence of limited immune inflammation
477 and anti-viral responses within the brain during viral infection. The observed changes in
478 immune gene expression warrant further comprehensive investigations to unravel the
479 underlying mechanisms and identify potential therapeutic targets within the brain.
480
481 **DISCUSSION**
482 **Neurotropism of SARS-CoV-2 and Behavioral Alterations**
483 Our findings revealed the presence of SARS-CoV-2 in the CNS, with viral dissemination
484 to the amygdala following intranasal inoculation in a sufficient SARS2-N501Y_{MA30}
485 infection mouse model **(Fig.1)**. These results are consistent with previous reports
486 indicating that SARS-CoV-2 can invade the human brain (5, 6), supporting the notion of
487 neurotropism. SARS-CoV-2 probably enters the central nervous system (CNS) through
488 two potential pathways (56). The first involves accessing the CNS via the neural-
489 mucosal interface in the olfactory mucosa, enabling the virus to spread from the
490 periphery olfactory neurons into the neurons of the olfactory bulb. The second pathway

491 is through entry into the brain via blood circulation, potentially breaching the blood-brain
492 barrier (BBB). In this scenario, the integrity of the BBB could be disrupted by
493 inflammatory responses triggered by the infection and/or infection of endothelial cells.
494
495 Notably, the observed viral invasion of the CNS was accompanied by significant
496 alterations in anxiety- and depression-like behaviors, as evidenced by behavioral
497 assays **(Fig. 2)**. Anxiety and depression are prevalent neuropsychiatric disorders
498 associated with significant morbidity and mortality worldwide. The link between other
499 viral infections and mental health disturbances has been reported in previous studies,
500 with evidence of viral neuroinvasion contributing to behavioral changes (57, 58). Our
501 study provides valuable evidence supporting a direct association between SARS-CoV-2
502 neurotropism and anxiety- and depression-like behaviors. These findings underscore
503 the importance of considering the potential neuropsychiatric consequences of COVID-
504 19 and highlight the need for comprehensive mental health assessments and
505 interventions during and after the acute phase of infection.
506
507 **Microglial Activation, Neuroinflammation, and Neuronal Activity**
508 Microglia, as the primary immune cells of the CNS, play a critical role in maintaining
509 brain homeostasis and protecting against infections (59). Upon encountering pathogens
510 or damage signals, microglia undergo rapid activation, transforming from a surveillant to
511 an immune-responsive phenotype. In our study, we observed robust microglial
512 activation in brain regions where viral particles were detected, suggesting a potential
513 role for microglia in mediating SARS-CoV-2-induced neurobehavioral alterations. While
514 microglia itself may not be a direct target of SARS-CoV-2 infection (4, 60), the initial
515 invasion of SARS-CoV-2 in the neuron cells of the brain likely triggers their activation.
516 Microglial activation can lead to neuroinflammation, characterized by the release of pro-
517 inflammatory cytokines, chemokines, and reactive oxygen species. Chronic
518 neuroinflammation has been implicated in the pathogenesis of various neuropsychiatric
519 disorders, including anxiety and depression (61). Notably, our transcriptomic analysis of
520 SARS-CoV-2-infected brains revealed upregulation of inflammatory and cytokine-
521 related pathways, supporting the hypothesis of microglia-driven neuroinflammation as a
522 mechanism underlying behavioral changes.
523
524 Based on our observations, we have formulated a hypothesis **(Fig. 7)** that SARS-CoV-2
525 targets neurons, leading to the release of ATP, a critical chemoattractant that activates
526 and attracts microglia (19, 52). This, in turn, can influence the activity of targeted
527 neurons through ATP-induced microglia activation (16, 17). Consequently, activated
528 microglia produce pro-inflammatory cytokines, further increasing neuronal activity and
529 resulting in alterations in anxiety- and depression-like behaviors. SARS-CoV-2 infection
530 has been shown to induce ATP release from host cells, including neural cells, through
531 ATP-release channels (54, 55), making ATP a fast responder to SARS2-N501Y$_{MA30}$
532 infection. Clinical and laboratory studies support the idea that cytokines may heighten
533 susceptibility to anxiety and depression (62), and they have been shown to upregulate
534 excitatory neuronal excitability and synaptic transmission (63). Increased levels of IL-1β,
535 IL-6, and TNF-α have also been associated with the development of anxiety and
536 depression-like behaviors in mice (64-66). These findings suggest that the

neuroinflammatory response triggered by SARS-CoV-2 infection may contribute to the changes observed in anxiety and depression-like behaviors in response to the virus infection.

Microglial Inhibition and Neuronal Activity Reversal

To elucidate the specific role of microglia in mediating neuronal activity following SARS-CoV-2 infection, we selectively inhibit microglia using a pharmacological approach. Intriguingly, microglial inhibition resulted in a significant attenuation of overexcited neuronal activity induced by viral spike protein. This observation indicates a direct involvement of microglia in the development of abnormal neuronal activity in response to SARS-CoV-2 infection. The observed neuronal activity rescue upon microglial inhibition aligns with previous studies showing that microglial activation is a key driver of neuronal activity changes in various CNS disorders (67). Understanding the interactions between microglia and neurons and how SARS-CoV-2 infection influences these processes in the amygdala is crucial to comprehending the neurological consequences of the virus. Such insights may offer valuable information to guide potential interventions or treatments for neurological manifestations observed in long COVID. Further research is needed to fully elucidate the intricate mechanisms underlying microglial activation and its impact on neuronal functions in response to SARS-CoV-2 infection in the brain.

Inflammatory Pathways and Therapeutic Interventions

The transcriptomic analysis of microglia from infected brains identified upregulated inflammatory pathways, suggesting potential targets for therapeutic interventions. This pharmacological approach further supports the role of microglia-driven neuroinflammation in the pathogenesis of SARS-CoV-2-induced behavioral alterations. Our study highlights the therapeutic potential of targeting neuroinflammatory pathways to ameliorate anxiety- and depression-like behaviors in COVID-19. Anti-inflammatory agents and immunomodulatory drugs that selectively dampen microglial activation may offer a promising avenue for treating the neuropsychiatric consequences of SARS-CoV-2 infection. However, further research is needed to identify specific inflammatory mediators and downstream signaling pathways responsible for the observed behavioral changes.

Limitations and Future Directions

While our study provides valuable insights into the link between SARS-CoV-2 neurotropism, microglial activation, neuronal activity, and anxiety- and depression-like behaviors, several limitations should be acknowledged. First, our study focused on the behaviors within weeks post-infection, and the longer effects of SARS-CoV-2 on mental health require further investigation. Additionally, we used a murine model, and findings in rodents may not fully translate to human conditions. Future research should explore the temporal dynamics of microglial activation and neuroinflammation throughout different stages of SARS-CoV-2 infection. Third, we identified that brain infection in mice developed mild to moderate respiratory diseases. We did not further evaluate the case of asymptomatic infection because a clinical study suggested that the risk of developing long-term symptoms in asymptomatic SARS-CoV-2 infected persons was significantly lower than those in symptomatic SARS-CoV-2 infection cases (68). Fourth, we utilized a

583 mouse-adapted SARS-CoV-2 strain that shares some key spike mutations with the Beta
584 variant. However, the specific potential, impact, and severity of neuroinvasion resulting
585 from different SARS-CoV-2 variants, such as the Omicron variant, and the potential
586 effects of breakthrough infections in vaccinated individuals, remain areas that require
587 further investigation to provide a comprehensive understanding. Fifth, we did not
588 systematically examine the role of respiratory COVID-19-induced cytokine/chemokine
589 elevation in microglia activation and its potential effects on CNS neuron function
590 impairment. It is well-established that exposure to chemotherapy drugs, brain radiation,
591 or systemic inflammation can lead to persistent activation of certain microglia (1, 69-72).
592 Interestingly, a recent study of SARS-CoV-2 infection in AAV-hACE2 sensitized mice or
593 H1N1 influenza infection in mice revealed that mild respiratory disease-activated white-
594 matter-selective microglia, leading to oligodendrocyte loss, impaired neurogenesis, and
595 elevated CCL11 levels (73). These findings highlight the potential impact of systemic
596 inflammation on microglia activation and brain function. Longitudinal studies in human
597 cohorts are necessary to establish causality between viral neurotropism, microglial
598 activation, and neuropsychiatric outcomes. Moreover, investigating potential sex-
599 dependent differences in behavioral responses and microglial activation can provide a
600 more comprehensive understanding of COVID-19-associated neuropsychiatric
601 sequelae. Addressing these limitations through further research is essential to advance
602 our understanding of the complex neurological effects of SARS-CoV-2 infection and its
603 variants. By delving deeper into these areas, we can gain valuable insights to develop
604 more effective interventions and treatment strategies for individuals affected by COVID-
605 19 and its neurological consequences.
606
607 **Conclusion**
608 In conclusion, our study demonstrates that SARS-CoV-2 neurotropism induces anxiety-
609 and depression-like behaviors through the activation of microglia and subsequent
610 neuroinflammation. These findings underscore the importance of considering mental
611 health disturbances in COVID-19 patients and emphasize the need for integrated
612 approaches to address both the physical and mental health aspects of the pandemic.
613 Targeting microglial activation and neuroinflammatory pathways may offer promising
614 therapeutic avenues to mitigate the neurobehavioral consequences of SARS-CoV-2
615 infection. Further investigations in human cohorts are warranted to validate and extend
616 our preclinical findings for potential translational applications.
617
618 **AUTHOR CONTRIBUTIONS**
619 J.D. and K.L. conceived the project. J.D., K.L., and Q.G. designed the experiments.
620 Q.G. and J.D. performed the patch-clamp and immunostaining experiments and data
621 analysis. S.Z. and K.L. performed the behavior and molecular experiments and data
622 analysis. K.L., J.D., and Q.G. wrote the manuscript. All authors reviewed and edited the
623 manuscript.
624
625 **ACKNOWLEDGMENTS**
626 J.D. is supported by the National Institutes of Mental Health (1R01MH113986), the
627 Cystic Fibrosis Foundation (002544I221), and the University of Tennessee Health

Science Center start-up fund. K.L. is supported by the Cystic Fibrosis Foundation and the Cleveland Clinic Florida Research and Innovation Center start-up fund.

CONFLICT-OF-INTEREST

The authors have declared that no conflict of interest exists.

FIGURE LEGENDS

Figure. 1. Outcomes of Intranasal Infection with a Mouse-Adapted SARS-CoV-2 Strain in Mice. (A) Schematic depicting the outcomes of infection in young BALB/c and C57BL/6 mice following administration of 10^4 PFU of SARS2-N501Y$_{MA30}$. **(B-C)** Daily monitoring of body weight (B) and survival (C) in young BALB/c and C57BL/6 mice post-infection. **(D-E)** Virus titers in the lungs (D) and brains (E) of C57BL/6 mice infected with SARS2-N501Y$_{MA30}$ at the indicated days post-infection. **(F-G)** Viral genomic RNA (gRNA) (F) and subgenomic RNA (sgRNA) (G) levels in brain tissues from SARS2-N501Y$_{MA30}$ infected C57BL/6 mice. The levels of viral gRNA and sgRNA were normalized to GAPDH and presented as 2^-ΔCT (n = 4 or 5 mice per group). CT values for viral genomic RNA (gRNA) or subgenomic RNA (sgRNA) from mock-infected tissues were consistently greater than 35. Statistical significance: ***p = 0.001, **p = 0.0017, determined by ordinary one-way ANOVA. **(H-J)** Immunofluorescence staining targeting dsRNA (red), neuronal nuclear protein (NeuN, green), and nuclei (DAPI, blue) in amygdala brain slices with mock infection (H) and at 4 or 14 days post-SARS2-N501Y$_{MA30}$ infection (I-J). Arrows indicate dsRNA and NeuN-positive neurons. Inserts show enlarged single-cell images. **(K)** Percentage of dsRNA-positive cells in slices from the amygdala and the prefrontal cortex (PFC). The peak of dsRNA-positive cells is observed at 4 dpi. Statistical significance: **p = 0.0012, determined by a two-tailed unpaired Student's t-test. Data are presented as mean ± SEM.

Figure. 2. Effects of SARS2-N501Y$_{MA30}$ on anxiety- and depression-like Behaviors in Mice. (A) Experimental design and timeline illustrating the administration of SARS2-N501Y$_{MA30}$ and the behavioral test battery. **(B)** Open field test. Upper: Representative heat map tracking of activity in the vehicle and SARS2-N501Y$_{MA30}$ infected mice. Lower: Results depicting the total travel distance and time spent in the center area. Statistical significance: **p = 0.0014 (total travel distance); ns, non-significant, p = 0.2927 (center area). **(C)** Elevated plus maze test. Upper: Representative heat map tracking of activity in mock and SARS2-N501Y$_{MA30}$ infected mice in closed arms (C) and open arms (O). Lower: Results indicating the time spent in open arms and the number of entries into open arms. Statistical significance: *p = 0.0299 (time spent in open arms); ns, non-significant, p = 0.6897 (number of entries). **(D-E)** Schematics of the tail suspension (D) and forced swimming (E) tests and results showing immobile time. Statistical significance: *p = 0.0118 (tail suspension test); **p = 0.0029 (forced swimming test). All statistical analyses were performed using a two-tailed unpaired Student's t-test. The analysis includes data from 10 mice in each group. Data are presented as mean ± SEM.

Figure. 3. Enhancement of Microglia-Dependent fEPSPs in the Amygdala by SARS-CoV-2 Variant B.1.351 Spike Protein. (A) Schematic representation of field excitatory postsynaptic potential (fEPSP) recording in brain slices. **(B)** Representative

674 fEPSP traces were recorded at the beginning (0 hours) and the end of the 2-hour
675 recordings, during perfusion with either vehicle or spike protein (S1+S2, B.1.351, β
676 variant, BPS Bioscience #510333, 200 ng/ml). **(C)** Average fEPSP data. The spike
677 protein was applied to the slice (200 ng/ml) at the indicated time point (red trace). In the
678 vehicle group, a mock aqueous buffer solution without the spike protein was used (gray
679 trace). The enhancement of fEPSPs by the spike protein was attenuated by pre-treating
680 brain slices with 50 μM Resveratrol (green trace). **(D)** Summarized amplitudes of the
681 last five fEPSPs as shown in (C). Statistical significance: ***p = 0.0003, **p = 0.0082,
682 determined by one-way ANOVA with Tukey's post hoc multiple comparisons. The
683 analysis includes data from 5 slices in each group. Data are presented as mean ± SEM.
684
685 **Figure. 4. Golgi-Cox Staining of Neurons in the Amygdala of SARS2-N501Y$_{MA30}$**
686 **Infected Mice. (A)** Experimental design and timeline depicting the administration of
687 SARS2-N501Y$_{MA30}$, dissection of brain slices, and Golgi staining process. **(B-C)** Left:
688 Representative Golgi-Cox staining images of amygdala slices from mock-infected (B)
689 and mice infected with SARS2-N501Y$_{MA30}$ at 14 days post-infection (dpi) (C). Scale bar
690 = 200 μm. Right: Enlarged images from the red boxes in the left images for each
691 respective group. Scale bar = 50 μm. **(D)** Representative dendrite images from the red
692 boxes in (B) and (C). Scale bar = 2 μm. **(E)** Comparison of the percentage of mature
693 spines in the mock and SARS2-N501Y$_{MA30}$ infection groups. Statistical significance: **p
694 = 0.0038 (t = 3.296, df = 19). The analysis includes data from 11 neurons sourced from
695 4 mice in each group. Statistical analysis was performed using a two-tailed unpaired
696 Student's t-test. Data are presented as mean ± SEM.
697
698 **Figure. 5. Microglial Activation in Response to SARS-CoV-2 infection and B1.351**
699 **Spike Protein. (A-C)** Immunofluorescence results using Iba1 (a microglia marker) show
700 the dynamics of microglial activation at different time points following virus infection (n =
701 4 per group*).* **(D-F)** Immunostaining with Iba-1, a microglia marker, depicting microglia in
702 brain slices following one-hour perfusion of the vehicle (D), the spike protein (E), or the
703 spike protein with a 30-minute pretreatment of 50 μM Ticlopidine (P2Y12R antagonist)
704 (F). **(G)** Comparison of microglial activation assessed by Sholl analysis, which
705 measures the total branch length and radius of cell area. Statistical significance: ****p <
706 0.0001, ***p = 0.0006, determined by one-way ANOVA with Tukey's post hoc multiple
707 comparisons. The analysis includes data from 30 cells across 4 slices in each group.
708 Data are presented as mean ± SEM. **(H)** Schematic outlines the experimental setup for
709 studying the release of ATP from brain slices induced by B1.351 spike protein. **(I)**
710 Quantification of ATP release. The amount of ATP released into the supernatant was
711 quantified. Each dot is an independent brain slice and represents the mean of 2
712 technical replicates. Statistical significance: *p < 0.05, ****p < 0.0001, determined by 2-
713 way ANOVA. Data are presented as mean ± SEM.
714
715 **Figure. 6. Cytokines and Chemokines Induced in the Brain of SARS-CoV-2-**
716 **Infected Mice.** Brains of C57BL/6 mice intranasally infected with 10^4 PFU of SARS2-
717 N501Y$_{MA30}$ were harvested at indicated days post-infection. Cytokine and chemokine
718 transcripts were measured by quantitative real-time PCR (qRT-PCR) analyzing total
719 RNA extracted from mock-infected (0 dpi) and infected young C57BL/6 mice. Each

720 brain was collected from an individual mouse. Mock (0 dpi), 2, 4, 8, 14 dpi: n=4; 6 dpi:
721 n=5. The levels of transcripts were normalized to GAPDH and presented as 2^-ΔCT.
722 Statistical significance: *p < 0.05, **p < 0.01, ****p < 0.0001, determined by ordinary
723 one-way ANOVA. Data are presented as mean ± SEM.
724
725 **Figure. 7. Schematic of a model of SARS2-N501Y$_{MA30}$ neurotropism-induced**
726 **anxiety and depression-like behaviors.** Our hypothesis centers on the possibility of
727 SARS-CoV-2 targeting neurons to induce the release of ATP, which in turn recruits and
728 activates microglia. This microglial activation may lead to the production of pro-
729 inflammatory cytokines, subsequently increasing neuronal activity and ultimately
730 influencing alterations in defensive behaviors.
731
732 **Supplemental Figure 1. SARS2-N501Y$_{MA30}$ Virus RNA Replication and Host**
733 **Immune Responses in the Lungs.** Lungs from C57BL/6 mice intranasally infected with
734 10^4 PFU of SARS2-N501Y$_{MA30}$ were harvested at specified days post-infection. Viral
735 RNA, as well as host cytokine and chemokine transcripts, were quantified using
736 quantitative real-time polymerase chain reaction (qRT-PCR), analyzing total RNA
737 extracted from both mock-infected (0 dpi) and virus-infected young C57BL/6 mice. Each
738 lung sample was obtained from an individual mouse. Sample sizes ranged from n=3 to
739 n=5. CT values of viral gRNA or sgRNA from mock-infected tissues were all >35.
740 Transcript levels were normalized to GAPDH and expressed as 2^-ΔCT. Statistical
741 significance was assessed using ordinary one-way ANOVA, with significance levels
742 indicated as follows: *p < 0.05, **p < 0.01, ***p < 0.001, ****p < 0.0001. Data are
743 presented as mean ± SEM.
744
745 **Supplemental Figure 2. Histopathology of Brain after Mock and SARS-CoV-2**
746 **Infection.** The representative images of brain tissue sections were stained with
747 hematoxylin and eosin (H&E) at indicated days following either mock or SARS-CoV-2
748 infection. Scale bar: 50 μm
749
750 **Supplemental Figure 3. Lung Pathology and Immunohistochemistry of Viral**
751 **Protein. (A)** Lung sections obtained from SARS2-N501YMA30-infected mice (n=5 for
752 mock infection and at 6 dpi; n=4 at 14 dpi) were subjected to H&E staining. **(B)** The
753 severity of acute lung injury was assessed through a blinded histopathological
754 evaluation of lung damage following ATS guidelines (31). An average score of 0
755 indicated the absence of injury, 1 indicated mild to moderate injury, and 2 indicated
756 severe injury. Scale bars: 100 μm. Data in (B) are presented as mean ± SEM. **(C)**
757 Representative images of lung tissue from mock-infected mice at indicated days post-
758 infection. Immunohistochemistry was employed to identify SARS-CoV-2-infected cells in
759 lung tissue sections from the indicated days post-infection. Tissues were
760 immunohistochemically stained (brown) for the SARS-CoV-2 N protein (black arrows).
761 Scale bar: 100 μm.
762
763 **Supplemental table 1. Quantitative real-time PCR analysis of viral RNA.**
764
765

766 **REFERENCES**

767 1. A. C. Geraghty *et al.*, Loss of Adaptive Myelination Contributes to Methotrexate
768 Chemotherapy-Related Cognitive Impairment. *Neuron* **103**, 250-265 e258
769 (2019).
770 2. Z. A. Sherif *et al.*, Pathogenic mechanisms of post-acute sequelae of SARS-
771 CoV-2 infection (PASC). *Elife* **12** (2023).
772 3. B. Bowe, Y. Xie, Z. Al-Aly, Postacute sequelae of COVID-19 at 2 years. *Nat Med*
773 **29**, 2347-2357 (2023).
774 4. M. G. Andrews *et al.*, Tropism of SARS-CoV-2 for human cortical astrocytes.
775 *Proc Natl Acad Sci U S A* **119**, e2122236119 (2022).
776 5. E. Song *et al.*, Neuroinvasion of SARS-CoV-2 in human and mouse brain. *J Exp*
777 *Med* **218** (2021).
778 6. S. R. Stein *et al.*, SARS-CoV-2 infection and persistence in the human body and
779 brain at autopsy. *Nature* **612**, 758-763 (2022).
780 7. M. F. DosSantos *et al.*, Neuromechanisms of SARS-CoV-2: A Review. *Front*
781 *Neuroanat* **14**, 37 (2020).
782 8. A. Pepe, S. Pietropaoli, M. Vos, G. Barba-Spaeth, C. Zurzolo, Tunneling
783 nanotubes provide a route for SARS-CoV-2 spreading. *Sci Adv* **8**, eabo0171
784 (2022).
785 9. M. G. Savelieff, E. L. Feldman, A. M. Stino, Neurological sequela and disruption
786 of neuron-glia homeostasis in SARS-CoV-2 infection. *Neurobiol Dis* **168**, 105715
787 (2022).
788 10. D. Davalos *et al.*, ATP mediates rapid microglial response to local brain injury in
789 vivo. *Nat Neurosci* **8**, 752-758 (2005).
790 11. A. Nimmerjahn, F. Kirchhoff, F. Helmchen, Resting microglial cells are highly
791 dynamic surveillants of brain parenchyma in vivo. *Science* **308**, 1314-1318
792 (2005).
793 12. R. M. Ransohoff, V. H. Perry, Microglial physiology: unique stimuli, specialized
794 responses. *Annu Rev Immunol* **27**, 119-145 (2009).
795 13. H. Wake, A. J. Moorhouse, S. Jinno, S. Kohsaka, J. Nabekura, Resting microglia
796 directly monitor the functional state of synapses in vivo and determine the fate of
797 ischemic terminals. *J Neurosci* **29**, 3974-3980 (2009).
798 14. M. E. Tremblay, R. L. Lowery, A. K. Majewska, Microglial interactions with
799 synapses are modulated by visual experience. *PLoS Biol* **8**, e1000527 (2010).
800 15. K. M. Lucin, T. Wyss-Coray, Immune activation in brain aging and
801 neurodegeneration: too much or too little? *Neuron* **64**, 110-122 (2009).
802 16. Q. Li, B. A. Barres, Microglia and macrophages in brain homeostasis and
803 disease. *Nat Rev Immunol* **18**, 225-242 (2018).
804 17. D. P. Schafer, E. K. Lehrman, B. Stevens, The "quad-partite" synapse: microglia-
805 synapse interactions in the developing and mature CNS. *Glia* **61**, 24-36 (2013).
806 18. D. J. Stein, M. F. Vasconcelos, L. Albrechet-Souza, K. M. M. Cereser, R. M. M.
807 de Almeida, Microglial Over-Activation by Social Defeat Stress Contributes to
808 Anxiety- and Depressive-Like Behaviors. *Front Behav Neurosci* **11**, 207 (2017).
809 19. U. B. Eyo *et al.*, Neuronal hyperactivity recruits microglial processes via neuronal
810 NMDA receptors and microglial P2Y12 receptors after status epilepticus. *J*
811 *Neurosci* **34**, 10528-10540 (2014).

812 20. A. M. Fontainhas *et al.*, Microglial morphology and dynamic behavior is regulated
813 by ionotropic glutamatergic and GABAergic neurotransmission. *PLoS One* **6**,
814 e15973 (2011).
815 21. Y. Li, X. F. Du, C. S. Liu, Z. L. Wen, J. L. Du, Reciprocal regulation between
816 resting microglial dynamics and neuronal activity in vivo. *Dev Cell* **23**, 1189-1202
817 (2012).
818 22. J. Damas *et al.*, Broad host range of SARS-CoV-2 predicted by comparative and
819 structural analysis of ACE2 in vertebrates. *Proc Natl Acad Sci U S A* **117**, 22311-
820 22322 (2020).
821 23. M. A. A. Mahdy, W. Younis, Z. Ewaida, An Overview of SARS-CoV-2 and Animal
822 Infection. *Front Vet Sci* **7**, 596391 (2020).
823 24. D. V. Glazkova *et al.*, Generation of SARS-CoV-2 Mouse Model by Transient
824 Expression of the Human ACE2 Gene Mediated by Intranasal Administration of
825 AAV-hACE2. *Mol Biol* **56**, 705-712 (2022).
826 25. J. Sun *et al.*, Generation of a Broadly Useful Model for COVID-19 Pathogenesis,
827 Vaccination, and Treatment. *Cell* **182**, 734-743 e735 (2020).
828 26. J. Zheng *et al.*, COVID-19 treatments and pathogenesis including anosmia in
829 K18-hACE2 mice. *Nature* **589**, 603-607 (2021).
830 27. L. R. Wong *et al.*, Eicosanoid signalling blockade protects middle-aged mice from
831 severe COVID-19. *Nature* **605**, 146-151 (2022).
832 28. P. H. Janak, K. M. Tye, From circuits to behaviour in the amygdala. *Nature* **517**,
833 284-292 (2015).
834 29. L. R. Wong *et al.*, Sensitization of Non-permissive Laboratory Mice to SARS-
835 CoV-2 with a Replication-Deficient Adenovirus Expressing Human ACE2. *STAR*
836 *Protoc* **1**, 100169 (2020).
837 30. J. Du *et al.*, Transient acidosis while retrieving a fear-related memory enhances
838 its lability. *Elife* **6** (2017).
839 31. G. Matute-Bello *et al.*, An official American Thoracic Society workshop report:
840 features and measurements of experimental acute lung injury in animals. *Am J*
841 *Respir Cell Mol Biol* **44**, 725-738 (2011).
842 32. F. Levet, J. Tonnesen, U. V. Nagerl, J. B. Sibarita, SpineJ: A software tool for
843 quantitative analysis of nanoscale spine morphology. *Methods* **174**, 49-55
844 (2020).
845 33. C. J. Kreple *et al.*, Acid-sensing ion channels contribute to synaptic transmission
846 and inhibit cocaine-evoked plasticity. *Nat Neurosci* **17**, 1083-1091 (2014).
847 34. W. J. Wright *et al.*, Silent synapses dictate cocaine memory destabilization and
848 reconsolidation. *Nat Neurosci* **23**, 32-46 (2020).
849 35. H. Shuai *et al.*, Emerging SARS-CoV-2 variants expand species tropism to
850 murines. *EBioMedicine* **73**, 103643 (2021).
851 36. F. Rigoli, M. Ewbank, T. Dalgleish, A. Calder, Threat visibility modulates the
852 defensive brain circuit underlying fear and anxiety. *Neurosci Lett* **612**, 7-13
853 (2016).
854 37. J. Oh *et al.*, SARS-CoV-2 spike protein induces cognitive deficit and anxiety-like
855 behavior in mouse via non-cell autonomous hippocampal neuronal death. *Sci*
856 *Rep* **12**, 5496 (2022).

857 38. C.-Y. Chen, Y.-C. Chou, Y.-P. Hsueh, SARS-CoV-2 D614 and G614 spike
858 variants impair neuronal synapses and exhibit differential fusion ability. *BioRxiv*
859 10.1101/2020.12.03.409763 (2020).
860 39. M. G. Frank *et al.*, SARS-CoV-2 spike S1 subunit induces neuroinflammatory,
861 microglial and behavioral sickness responses: Evidence of PAMP-like properties.
862 *Brain Behav Immun* **100**, 267-277 (2022).
863 40. G. Datta *et al.*, SARS-CoV-2 S1 Protein Induces Endolysosome Dysfunction and
864 Neuritic Dystrophy. *Front Cell Neurosci* **15**, 777738 (2021).
865 41. S. Zhang *et al.*, Resveratrol Attenuates Microglial Activation via SIRT1-SOCS1
866 Pathway. *Evid Based Complement Alternat Med* **2017**, 8791832 (2017).
867 42. K. M. Woolfrey, D. P. Srivastava, Control of Dendritic Spine Morphological and
868 Functional Plasticity by Small GTPases. *Neural Plast* **2016**, 3025948 (2016).
869 43. G. Yang, F. Pan, W. B. Gan, Stably maintained dendritic spines are associated
870 with lifelong memories. *Nature* **462**, 920-924 (2009).
871 44. J. N. Bourne, K. M. Harris, Balancing structure and function at hippocampal
872 dendritic spines. *Annu Rev Neurosci* **31**, 47-67 (2008).
873 45. C. H. Bailey, E. R. Kandel, K. M. Harris, Structural Components of Synaptic
874 Plasticity and Memory Consolidation. *Cold Spring Harb Perspect Biol* **7**, a021758
875 (2015).
876 46. A. Peters, I. R. Kaiserman-Abramof, The small pyramidal neuron of the rat
877 cerebral cortex. The perikaryon, dendrites and spines. *Am J Anat* **127**, 321-355
878 (1970).
879 47. K. P. Berry, E. Nedivi, Spine Dynamics: Are They All the Same? *Neuron* **96**, 43-
880 55 (2017).
881 48. E. E. Koffman *et al.*, Acid-sensing ion channel 1a regulates the specificity of
882 reconsolidation of conditioned threat responses. *JCI Insight*
883 10.1172/jci.insight.155341 (2022).
884 49. A. Vidal-Itriago *et al.*, Microglia morphophysiological diversity and its implications
885 for the CNS. *Front Immunol* **13**, 997786 (2022).
886 50. M. Colonna, O. Butovsky, Microglia Function in the Central Nervous System
887 During Health and Neurodegeneration. *Annu Rev Immunol* **35**, 441-468 (2017).
888 51. S.-S. Lin, Y. Tang, P. Illes, A. Verkhratsky, The Safeguarding Microglia: Central
889 Role for P2Y12 Receptors. *Frontiers in Pharmacology* **11** (2021).
890 52. L. J. Wu, K. I. Vadakkan, M. Zhuo, ATP-induced chemotaxis of microglial
891 processes requires P2Y receptor-activated initiation of outward potassium
892 currents. *Glia* **55**, 810-821 (2007).
893 53. R. D. Fields, Nonsynaptic and nonvesicular ATP release from neurons and
894 relevance to neuron-glia signaling. *Semin Cell Dev Biol* **22**, 214-219 (2011).
895 54. R. Luu *et al.*, Pannexin-1 channel opening is critical for COVID-19 pathogenesis.
896 *iScience* **24**, 103478 (2021).
897 55. D. E. Ribeiro *et al.*, Hyperactivation of P2X7 receptors as a culprit of COVID-19
898 neuropathology. *Mol Psychiatry* **26**, 1044-1059 (2021).
899 56. S. M. Burks, H. Rosas-Hernandez, M. Alejandro Ramirez-Lee, E. Cuevas, J. C.
900 Talpos, Can SARS-CoV-2 infect the central nervous system via the olfactory bulb
901 or the blood-brain barrier? *Brain Behav Immun* **95**, 7-14 (2021).

57. K. Tomonaga, Virus-induced neurobehavioral disorders: mechanisms and implications. *Trends Mol Med* **10**, 71-77 (2004).
58. I. Kotsiri *et al.*, Viral Infections and Schizophrenia: A Comprehensive Review. *Viruses* **15** (2023).
59. M. E. Tremblay, C. Madore, M. Bordeleau, L. Tian, A. Verkhratsky, Neuropathobiology of COVID-19: The Role for Glia. *Front Cell Neurosci* **14**, 592214 (2020).
60. D. Beckman *et al.*, SARS-CoV-2 infects neurons and induces neuroinflammation in a non-human primate model of COVID-19. *Cell Rep* **41**, 111573 (2022).
61. S. J. Rhie, E. Y. Jung, I. Shim, The role of neuroinflammation on pathogenesis of affective disorders. *J Exerc Rehabil* **16**, 2-9 (2020).
62. N. Vogelzangs, P. de Jonge, J. H. Smit, S. Bahn, B. W. Penninx, Cytokine production capacity in depression and anxiety. *Transl Psychiatry* **6**, e825 (2016).
63. M. Schafers, L. Sorkin, Effect of cytokines on neuronal excitability. *Neurosci Lett* **437**, 188-193 (2008).
64. S. Rossi *et al.*, Interleukin-1beta causes anxiety by interacting with the endocannabinoid system. *J Neurosci* **32**, 13896-13905 (2012).
65. R. K. Farooq, K. Asghar, S. Kanwal, A. Zulqernain, Role of inflammatory cytokines in depression: Focus on interleukin-1beta. *Biomed Rep* **6**, 15-20 (2017).
66. M. A. Alshammari *et al.*, Systemic TNF-alpha blockade attenuates anxiety and depressive-like behaviors in db/db mice through downregulation of inflammatory signaling in peripheral immune cells. *Saudi Pharm J* **28**, 621-629 (2020).
67. J. Qin, Z. Ma, X. Chen, S. Shu, Microglia activation in central nervous system disorders: A review of recent mechanistic investigations and development efforts. *Front Neurol* **14**, 1103416 (2023).
68. Y. Ma *et al.*, Long-Term Consequences of Asymptomatic SARS-CoV-2 Infection: A Systematic Review and Meta-Analysis. *Int J Environ Res Public Health* **20** (2023).
69. E. M. Gibson *et al.*, Methotrexate Chemotherapy Induces Persistent Tri-glial Dysregulation that Underlies Chemotherapy-Related Cognitive Impairment. *Cell* **176**, 43-55 e13 (2019).
70. M. L. Monje, S. Mizumatsu, J. R. Fike, T. D. Palmer, Irradiation induces neural precursor-cell dysfunction. *Nat Med* **8**, 955-962 (2002).
71. M. L. Monje, H. Toda, T. D. Palmer, Inflammatory blockade restores adult hippocampal neurogenesis. *Science* **302**, 1760-1765 (2003).
72. M. L. Monje *et al.*, Impaired human hippocampal neurogenesis after treatment for central nervous system malignancies. *Ann Neurol* **62**, 515-520 (2007).
73. A. Fernandez-Castaneda *et al.*, Mild respiratory COVID can cause multi-lineage neural cell and myelin dysregulation. *Cell* **185**, 2452-2468 e2416 (2022).

Figure. 1

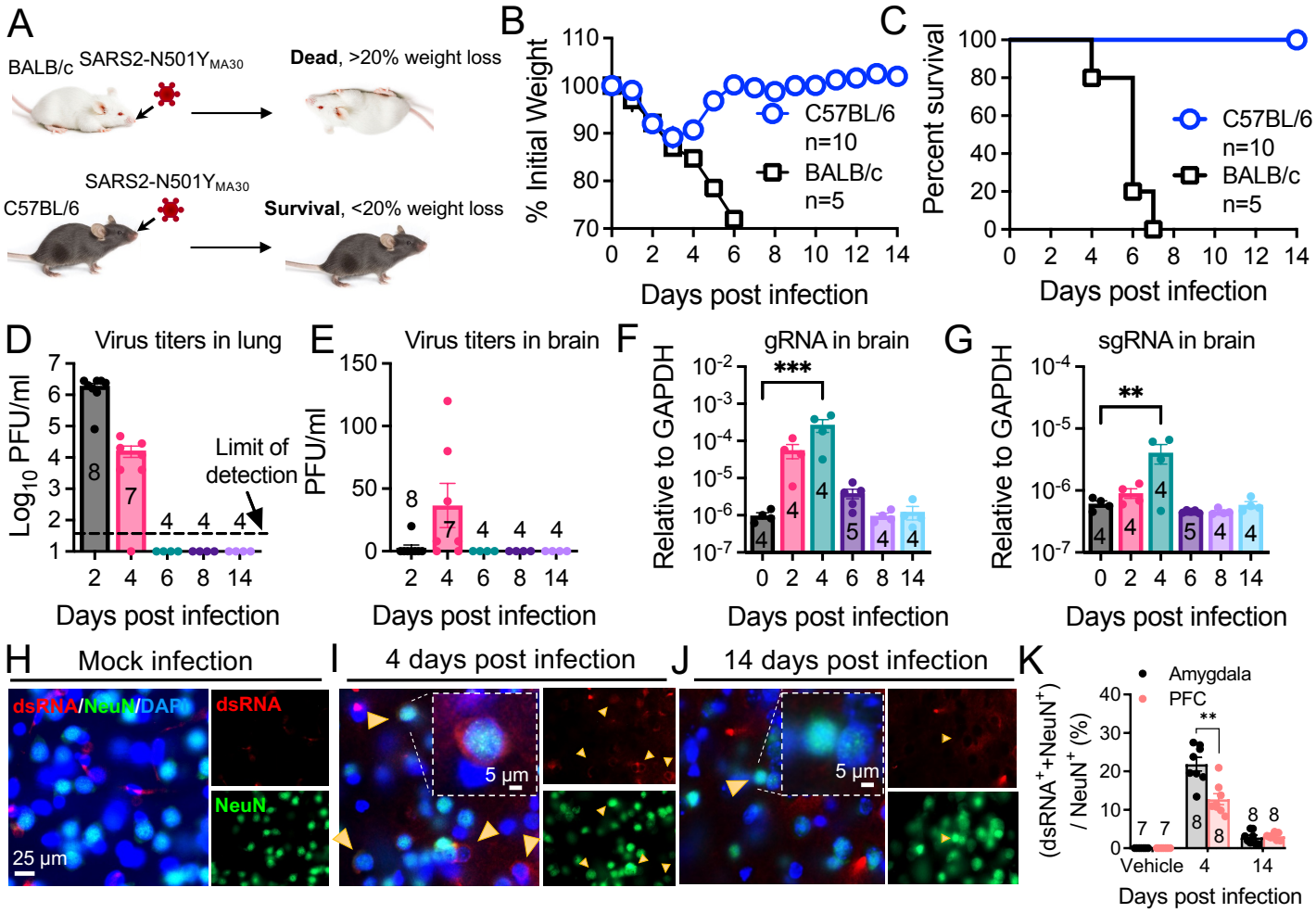
A
BALB/c
SARS2-N501Y$_{MA30}$
Dead, >20% weight loss
C57BL/6
SARS2-N501Y$_{MA30}$
Survival, <20% weight loss
B
% Initial Weight
C57BL/6
n=10
BALB/c
n=5
Days post infection
C
Percent survival
C57BL/6
n=10
BALB/c
n=5
Days post infection
D
Virus titers in lung
Log$_{10}$ PFU/ml
Limit of detection
Days post infection
E
Virus titers in brain
PFU/ml
Days post infection
F
gRNA in brain
Relative to GAPDH
***
Days post infection
G
sgRNA in brain
Relative to GAPDH
**
Days post infection
H
Mock infection
dsRNA/NeuN/DAPI
dsRNA
NeuN
25 μm
I
4 days post infection
5 μm
J
14 days post infection
5 μm
K
Amygdala
PFC
(dsRNA$^+$+NeuN$^+$) / NeuN$^+$ (%)
**
Vehicle
Days post infection

Figure. 2

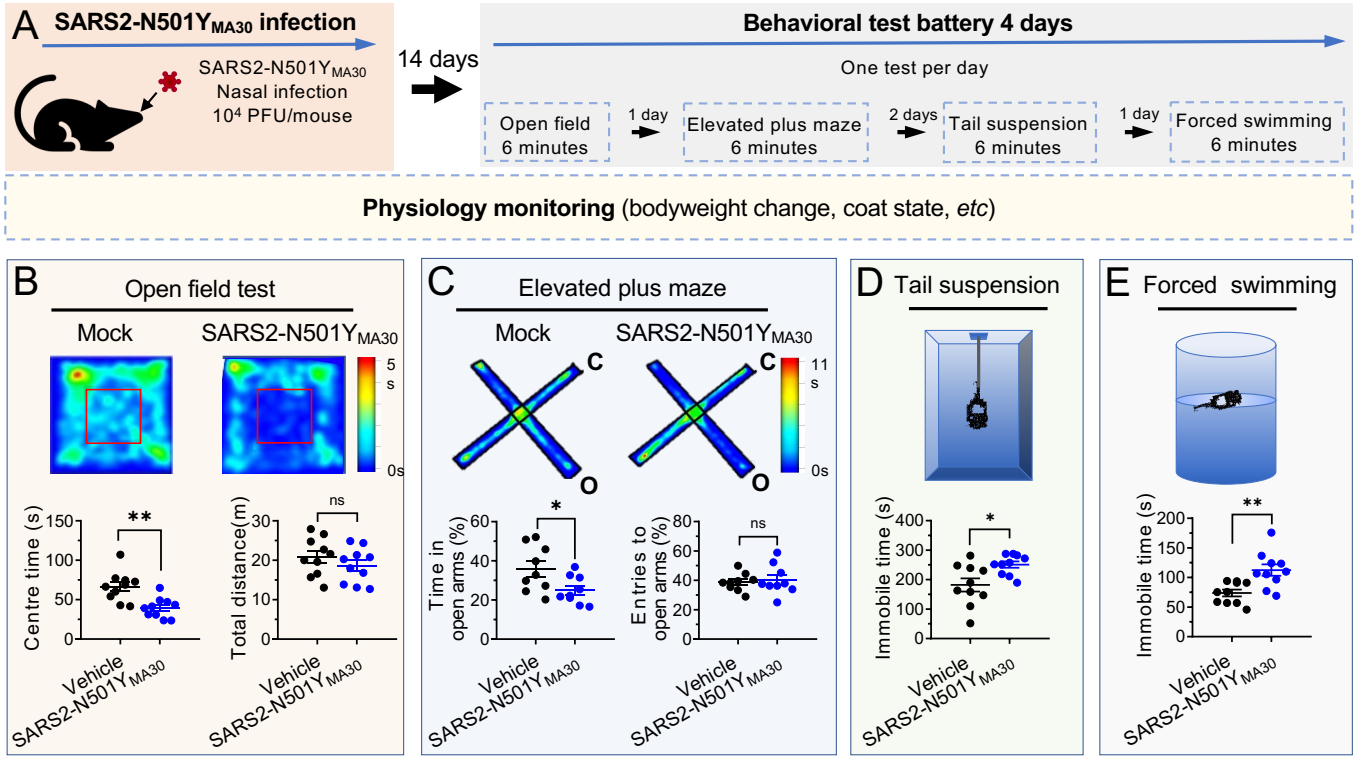
A SARS2-N501YMA30 infection
SARS2-N501YMA30
Nasal infection
10⁴ PFU/mouse
14 days
Behavioral test battery 4 days
One test per day
Open field 6 minutes
1 day
Elevated plus maze 6 minutes
2 days
Tail suspension 6 minutes
1 day
Forced swimming 6 minutes
Physiology monitoring (bodyweight change, coat state, etc)
B Open field test
Mock
SARS2-N501YMA30
5 s
0s
Centre time (s)
Total distance(m)
**
ns
Vehicle
SARS2-N501YMA30
C Elevated plus maze
Mock
SARS2-N501YMA30
C
O
11 s
0s
Time in open arms (%)
Entries to open arms (%)
*
ns
Vehicle
SARS2-N501YMA30
D Tail suspension
Immobile time (s)
*
Vehicle
SARS2-N501YMA30
E Forced swimming
Immobile time (s)
**
Vehicle
SARS2-N501YMA30

Figure. 3

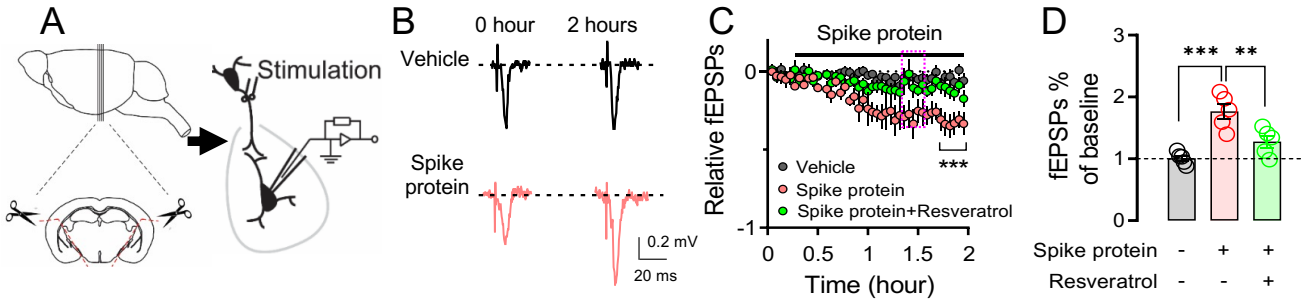
A
Stimulation
B
0 hour
2 hours
Vehicle
Spike protein
0.2 mV
20 ms
C
Spike protein
Relative fEPSPs
0
-1
***
Vehicle
Spike protein
Spike protein+Resveratrol
0
0.5
1
1.5
2
Time (hour)
D
fEPSPs % of baseline
3
2
1
0
***
**
Spike protein - + +
Resveratrol - - +

Figure. 4

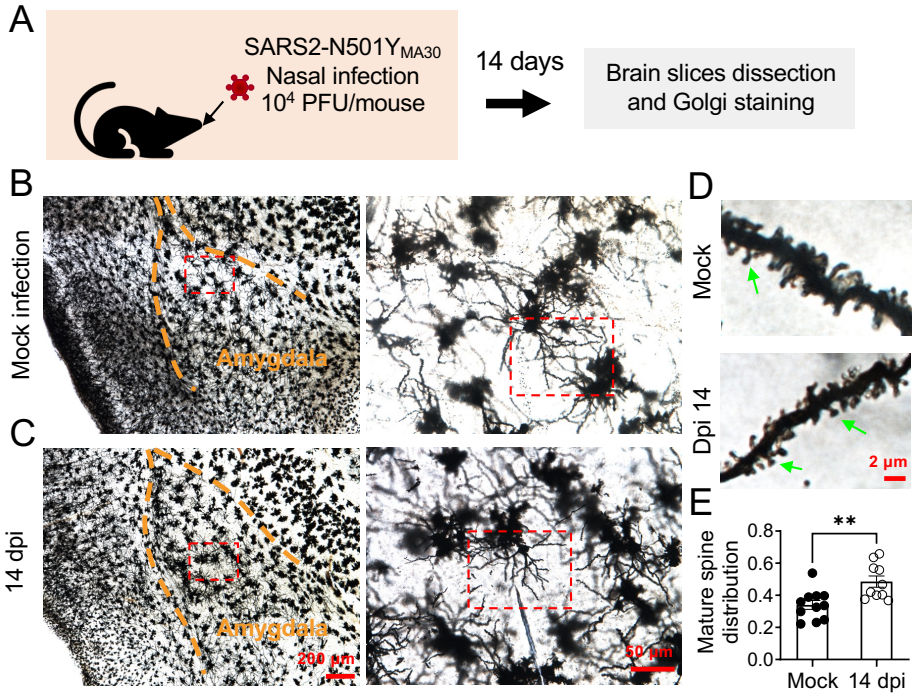
A
SARS2-N501Y$_{MA30}$
Nasal infection
10^4 PFU/mouse
14 days
Brain slices dissection
and Golgi staining
B
Mock infection
Amygdala
C
14 dpi
Amygdala
200 μm
50 μm
D
Mock
Dpi 14
2 μm
E
Mature spine distribution
0.8
0.6
0.4
0.2
0.0
**
Mock
14 dpi

Figure. 5

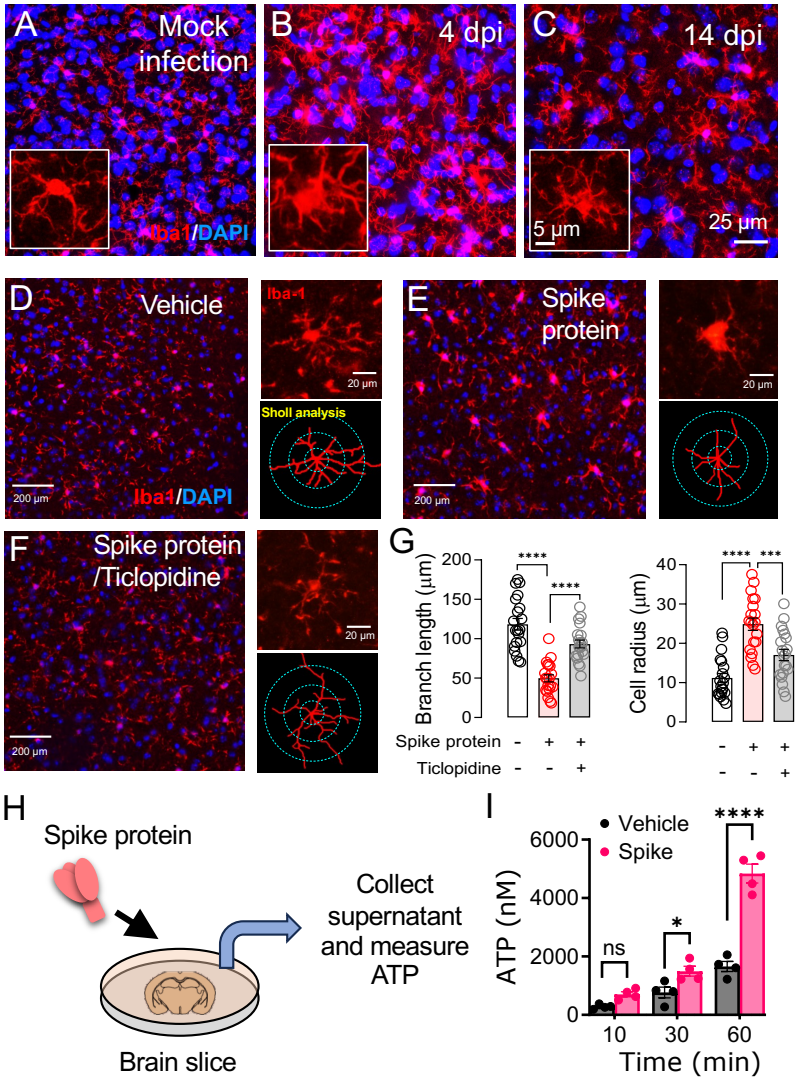
A
Mock infection
Iba1/DAPI
B
4 dpi
C
14 dpi
5 μm
25 μm
D
Vehicle
Iba-1
Sholl analysis
200 μm
20 μm
Iba1/DAPI
E
Spike protein
F
Spike protein /Ticlopidine
G
Branch length (μm)
Cell radius (μm)
Spike protein
Ticlopidine
H
Spike protein
Brain slice
Collect supernatant and measure ATP
I
Vehicle
Spike
ATP (nM)
Time (min)
ns
*
****

Figure. 6

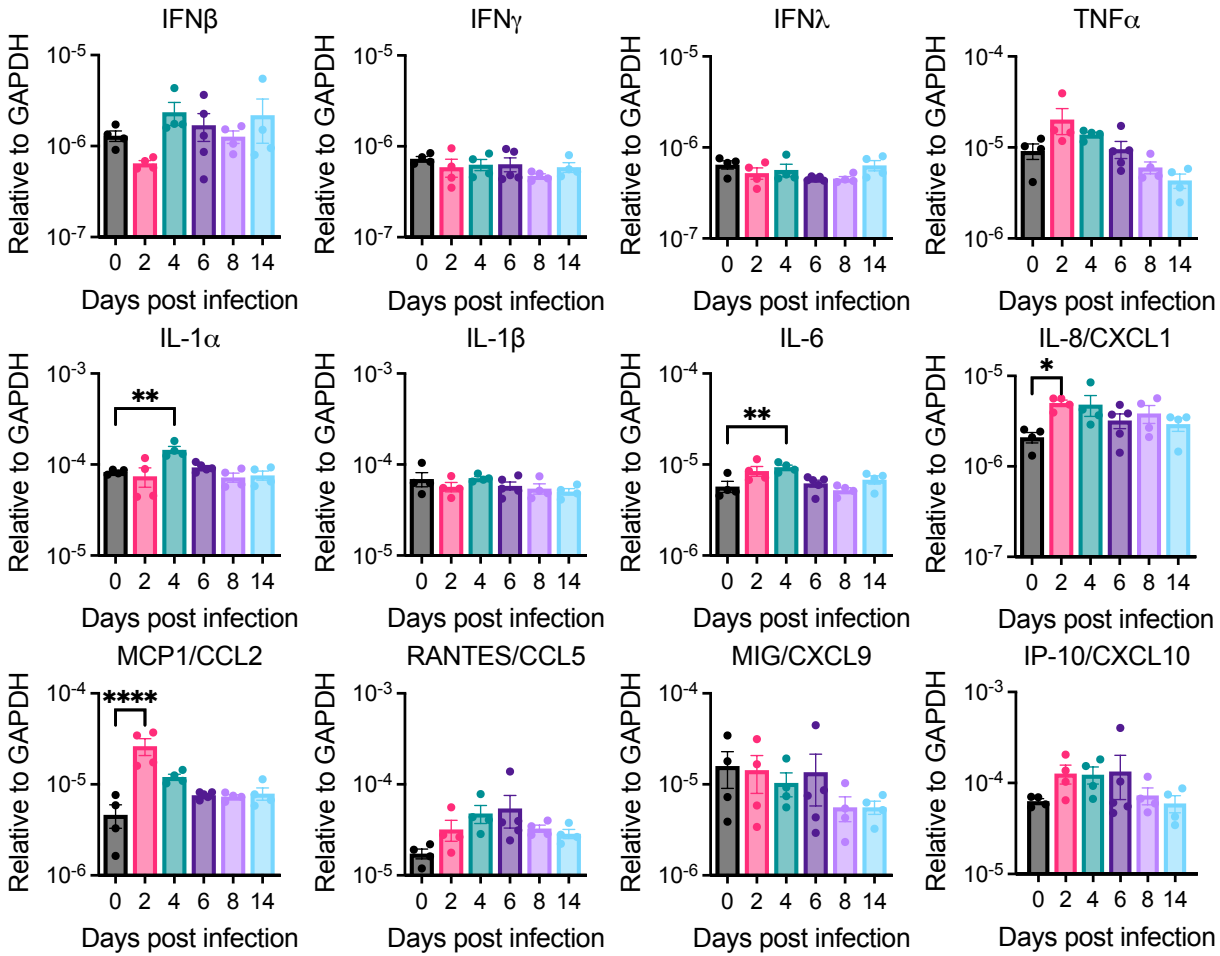
IFNβ
IFNγ
IFNλ
TNFα
IL-1α
IL-1β
IL-6
IL-8/CXCL1
MCP1/CCL2
RANTES/CCL5
MIG/CXCL9
IP-10/CXCL10
Relative to GAPDH
Days post infection
0 2 4 6 8 14
**
*
****

Figure. 7

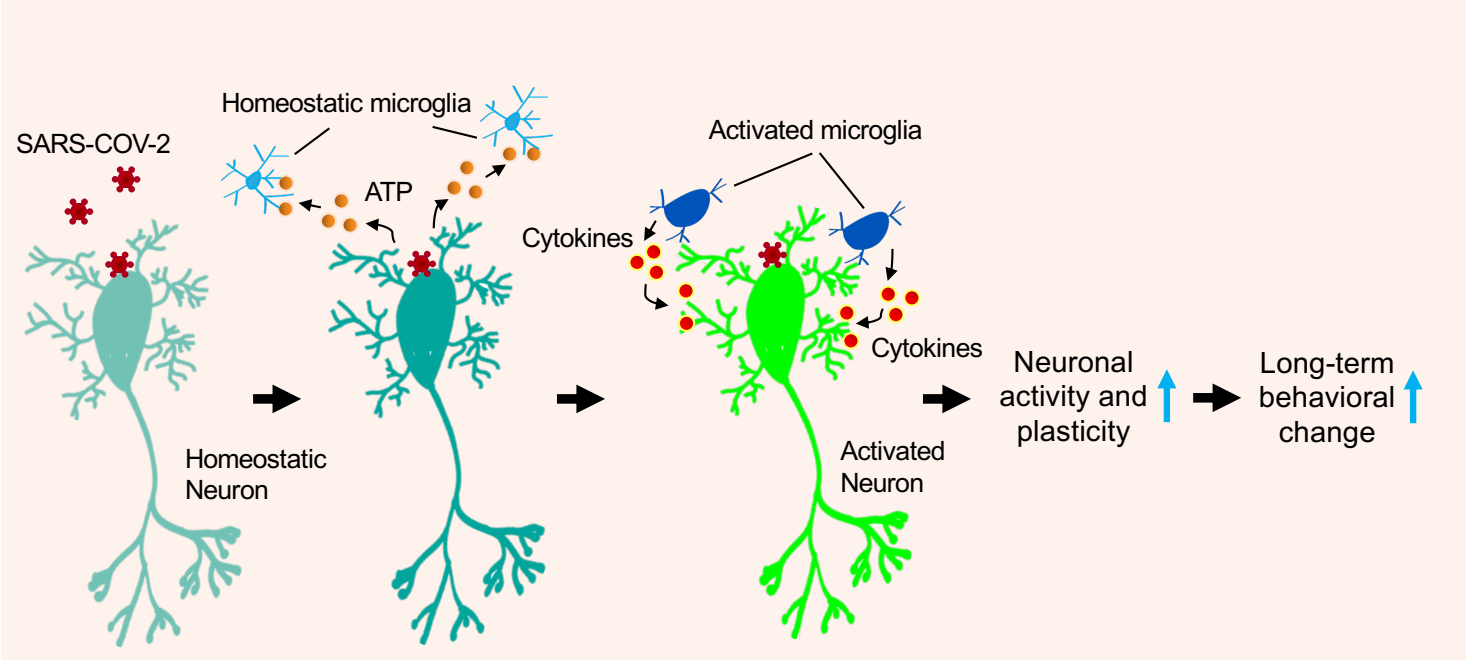
SARS-COV-2
Homeostatic microglia
ATP
Activated microglia
Cytokines
Cytokines
Homeostatic
Neuron
Activated
Neuron
Neuronal
activity and
plasticity
Long-term
behavioral
change

Supple Figure. 1

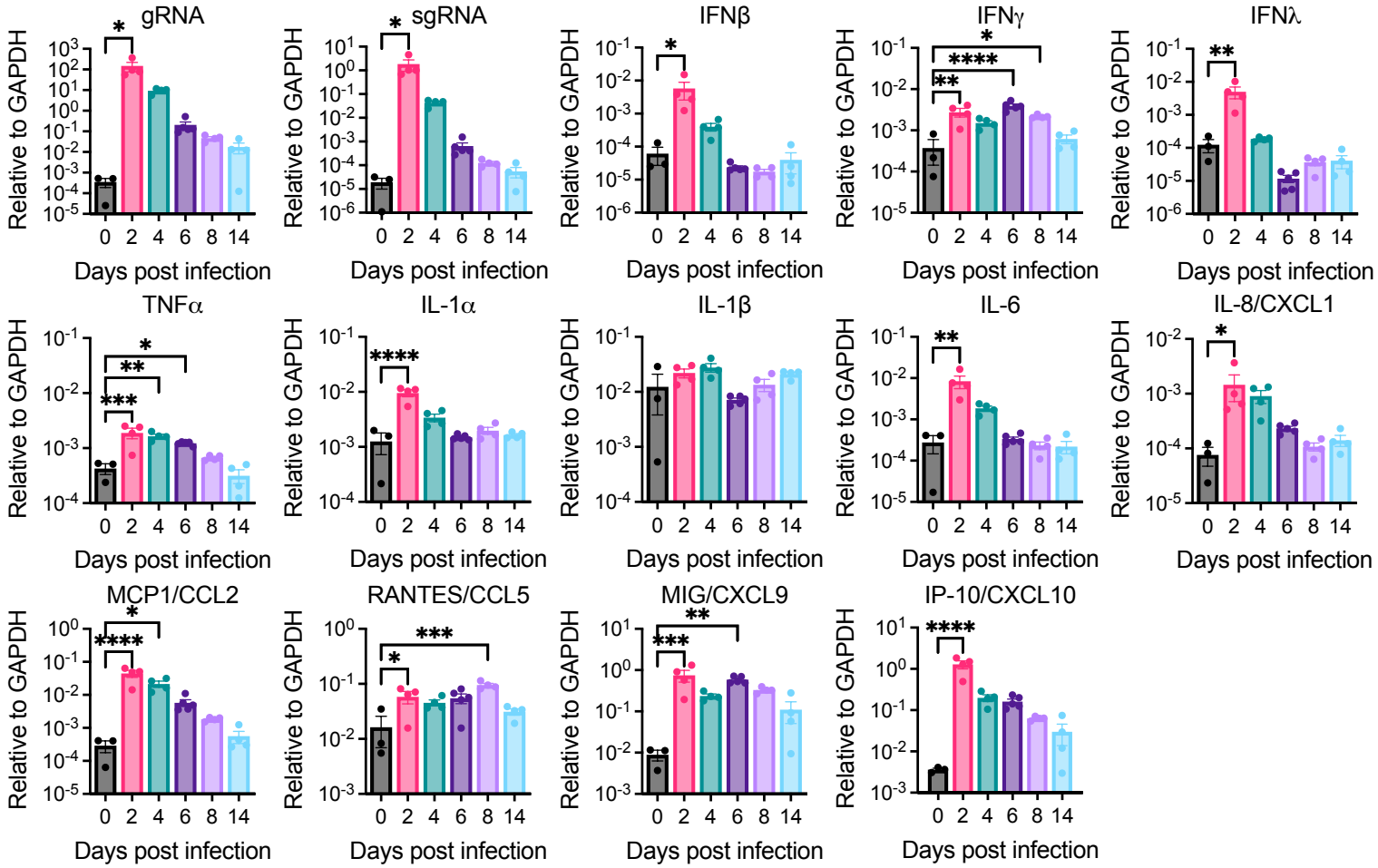

Supple Figure. 2

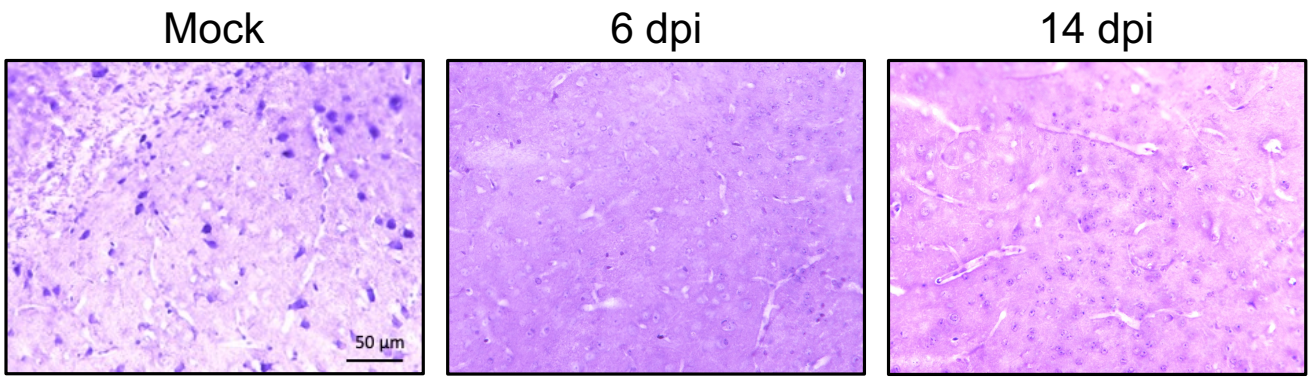

Supple Figure. 3

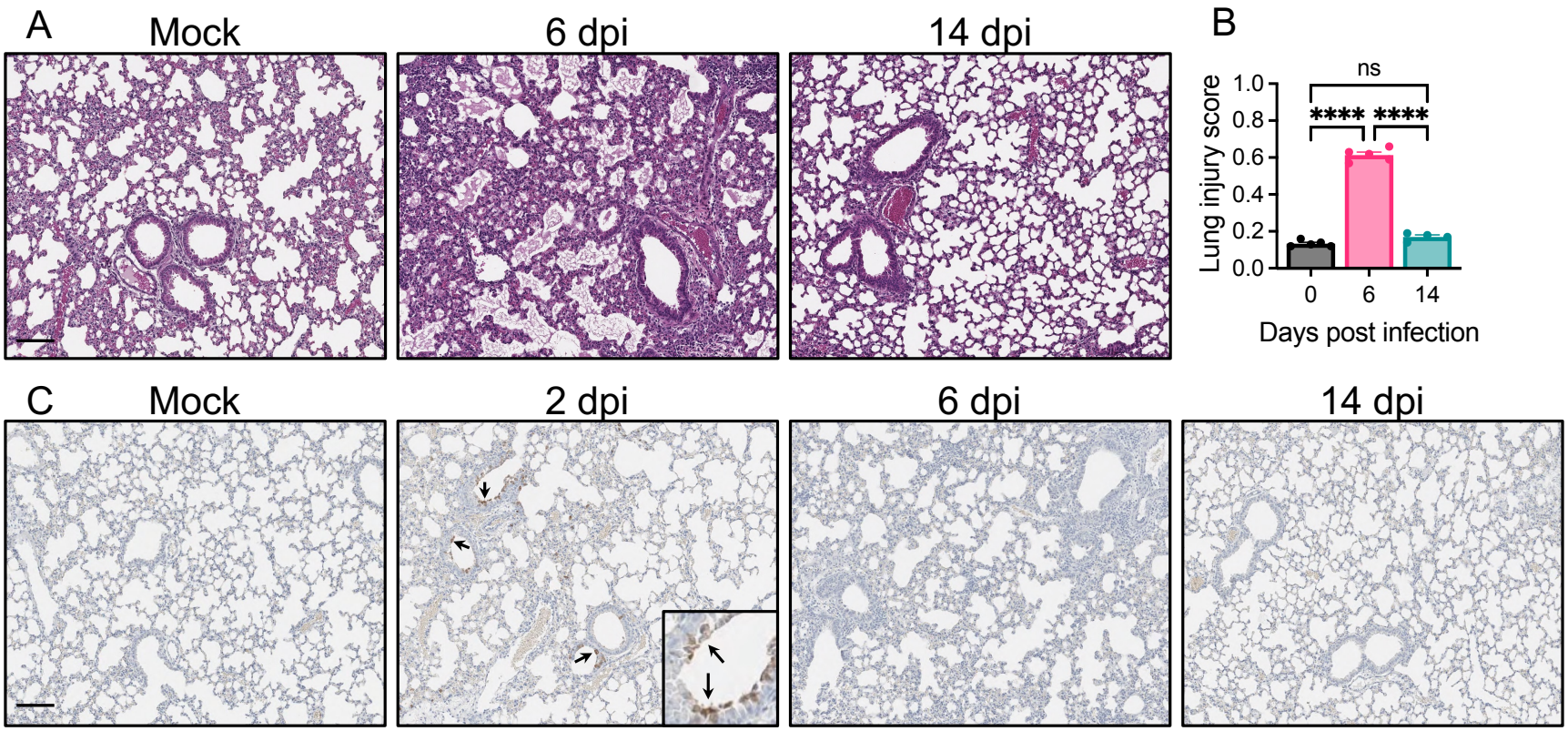

S1 Table. Quantitative real-time PCR analysis of viral RNA

Gene	Forward Primer	Reverse Primer
2019-nCoV_N1	GACCCCAAAATCAGCGAAAT	TCTGGT TACTGCCAGTTGAATCTG
SARS-CoV-2 sgRNA for E	CGATCTCTTGTAGATCTGTTCTC	ATATTGCAGCAGTACGCACACA
mGAPDH	AACAGCAACTCCCACTCTTC	CCTGTTGCTGTAGCCGTATT
mIFNβ	TCAGAATGAGTGGTGGTTGC	GACCTTTCAAATGCAGTAGATTCA
mIFNγ	CGGCACAGTCATTGAAAGCCTA	GTTGCTGATGGCCTGATTGTC
mIFNλ	AGCTGCAGGTCCAAGAGCG	GGTGGTCAGGGCTGAGTCATT
mTNFα	GAACTGGCAGAAGAGGCACT	AGGGTCTGGGCCATAGAACT
mIL1a	CGCTTGAGTCGGCAAAGAAAT	ACAAACTGATCTGTGCAAGTCTC
mIL-1b	ACTGTTTCTAATGCCTTCCC	ATGGTTTCTTGTGACCCTGA
mIL-6	GAGGATACCACTCCCAACAGACC	AAGTGCATCATCGTTGTTCATACA
mIL-8	CACCTCAAGAACATCCAGAGCT	CAAGCAGAACTGAACTACCATCG
mCCL2	CTTCTGGGCCTGCTGTTCA	CCAGCCTACTCATTGGGATCA
mCCL5	AGATCTCTGCAGCTGCCCTCA	GGAGCACTTGCTGCTGGTGTAG
mCXCL9	GCCATGAAGTCCGCTGTTCT	GGGTTCCTCGAACTCCACACT
mCXCL10	GCCGTCATTTTCTGCCTCAT	GCTTCCCTATGGCCCTCATT